NEOPLASIA
www.neoplasia.com

Volume 21 Number 1 January 2019 pp. 17–29 17

Characterizing Trastuzumab-Induced Alterations in Intratumoral Heterogeneity with Quantitative Imaging and Immunohistochemistry in HER2+ Breast Cancer

Anum K. Syed[*], Ryan Woodall[*], Jennifer G. Whisenant[†], Thomas E. Yankeelov[*,‡,§,¶,#] and Anna G. Sorace[*,‡,§,#]

[*]Department of Biomedical Engineering, The University of Texas at Austin, Austin, TX 78712; [†]Department of Medicine, Vanderbilt University Medical Center, Nashville, TN 37232; [‡]Department of Diagnostic Medicine, The University of Texas at Austin, Austin, TX 78712; [§]Department of Oncology, The University of Texas at Austin, Austin, TX 78712; [¶]Institute for Computational Engineering and Sciences, The University of Texas at Austin, Austin, TX 78712; [#]Livestrong Cancer Institutes, The University of Texas at Austin, Austin, TX 78712

Abstract

The purpose of this study is to investigate imaging and histology-based measurements of intratumoral heterogeneity to evaluate early treatment response to targeted therapy in a murine model of HER2+ breast cancer. BT474 tumor-bearing mice ($N = 30$) were treated with trastuzumab or saline and imaged longitudinally with either dynamic contrast-enhanced (DCE) magnetic resonance imaging (MRI) or ^{18}F-fluoromisonidazole (FMISO) positron emission tomography (PET). At the imaging study end point (day 4 for MRI or 7 for PET), each tumor was excised for immunohistochemistry analysis. Voxel-based histogram analysis was performed on imaging-derived parametric maps (i.e., K^{trans} and v_e from DCE-MRI, SUV from ^{18}F-FMISO-PET) of the tumor region of interest to measure heterogeneity. Image processing and histogram analysis of whole tumor slice immunohistochemistry data were performed to validate the *in vivo* imaging findings. Trastuzumab-treated tumors had increased heterogeneity in quantitative imaging measures of cellularity (v_e), with a mean Kolmogorov-Smirnov (K-S) distance of 0.32 ($P = .05$) between baseline and end point distributions. Trastuzumab-treated tumors had increased vascular heterogeneity (K^{trans}) and decreased hypoxic heterogeneity (SUV), with a mean K-S distance of 0.42 ($P < .01$) and 0.46 ($P = .047$), respectively, between baseline and study end points. These observations were validated by whole-slice immunohistochemistry analysis with mean interquartile range of CD31 distributions of 1.72 for treated and 0.95 for control groups ($P = .02$). Quantitative longitudinal changes in tumor cellular and vascular heterogeneity in response to therapy may provide evidence for early prediction of response and guide therapy for patients with HER2+ breast cancer.

Neoplasia (2019) 21, 17–29

Introduction

Intratumoral heterogeneity refers to the cellular diversity and regional differences in the microenvironment within a tumor. These variations can be phenotypic or genotypic in nature and are defined as a diverse collection of subpopulations within a single tumor [1,2]. Heterogeneity describes the nonuniform distribution of these subpopulations and the resulting alterations to the tumor microenvironment. For example, diverse proliferation rates and metabolic activity of cancer

Address all correspondence to: Anna G. Sorace, PhD, Department of Diagnostic Medicine, Dell Medical School, 1501 Red River St, The University of Texas at Austin, Austin, TX 78701. E-mail: anna.sorace@austin.utexas.edu
Received 22 August 2018; Revised 24 October 2018; Accepted 29 October 2018

© 2018 The Authors. Published by Elsevier Inc. on behalf of Neoplasia Press, Inc. This is an open access article under the CC BY-NC-ND license (http://creativecommons.org/licenses/by-nc-nd/4.0/).
1476-5586
https://doi.org/10.1016/j.neo.2018.10.008

cells, a characteristic of intratumoral heterogeneity, lead to varied regions of cellular density causing gradients in nutrient concentration and pH levels across the tumor microenvironment [3–5]. Furthermore, variations in quality and distribution of vasculature within a tumor, another characteristic of intratumoral heterogeneity, lead to the formation of hypoxic niches and result in nonuniform drug delivery, contributing to the rise of more resistant and aggressive disease [3,5,6]. Increased intratumoral heterogeneity is associated with variable treatment response and poorer patient prognosis [5,7] and provides a significant challenge to maximizing the efficacy of treatment as it adversely affects tumor response to therapies and increases the manifestation of resistant disease [1,8,9].

Approximately 20% of breast cancer cases in the United States are diagnosed as human epidermal growth factor receptor 2 positive (HER2+), a subtype of breast cancer associated with decreased pathological response rates to treatment, a heightened level of metastatic potential, and more aggressive disease compared to other breast cancer subtypes [10–13]. While HER2+ patients are identified by HER2 overexpression, heterogeneous distributions of intratumoral HER2 expression are often observed [14,15], contributing to varied manifestation of disease across patients. Trastuzumab, a monoclonal anti-HER2 antibody, is a targeted therapy used in the treatment of HER2+ breast cancer and has led to reduced recurrence of disease and dramatic improvements in patient survival [12,16,17]. In addition to its cytotoxic mechanisms, trastuzumab has been shown to alter tumor vasculature and oxygenation as a secondary mechanism of action [18–21]. Although trastuzumab has improved the treatment of locally advanced HER2+ breast cancer, only 30% of patients respond effectively to trastuzumab therapy in combination with other standard-of-care treatments [12,16,22,23]. For those patients who do not respond to therapy, earlier predictive measures of treatment response have the potential to optimally guide interventions, thereby improving outcomes while reducing exposure to ineffective treatments.

Methods to characterize tumor heterogeneity from noninvasive imaging data have recently been investigated to elucidate responses to treatment [7]. Clinically, qualitative descriptions often describe aspects of tumor heterogeneity from images, such as radiotracer "hot-spots" [24] or morphological descriptors regarding lesion spiculation [25,26]. However, these descriptions are subjective to observer evaluation of the tumor [7,24]. Signal intensity histogram analysis [27–29] and image texture analysis [30–33] are more quantitative methods used to characterize intratumoral heterogeneity in anatomical magnetic resonance imaging (MRI) data and computed tomography (CT) data. However, anticancer treatment interventions alter cellular and microenvironment heterogeneity, and these techniques often do not directly describe the biological heterogeneity present within the tumor. Additionally, initial changes in tumor microenvironment heterogeneity after treatment could serve as an early metric for treatment response and be used to guide therapy. Quantitative imaging strategies, such as dynamic contrast-enhanced (DCE) MRI [34] and ^{18}F-fluoromisonidazole (^{18}F-FMISO) positron emission tomography (PET) [35,36], can noninvasively and longitudinally measure biological and molecular tumor microenvironment alterations throughout anticancer treatment strategies [37–39]. DCE-MRI can be used to quantitatively characterize tissue vascular features related to blood flow, vessel permeability, and tissue volume fractions, parameters which have demonstrated the ability to predict treatment response in both preclinical [40–42] and clinical [43–45] studies of breast cancer. ^{18}F-FMISO-PET can noninvasively measure hypoxia through evaluation of the radiotracer uptake within the tumor and has been studied as a metric for early treatment response in preclinical models of breast cancer [18,46]. Parametric maps extracted from DCE-MRI and ^{18}F-FMISO-PET imaging provide voxel-level quantitative data of vasculature, cellularity, and oxygenation, thereby characterizing variability across the 3D tumor volume. Currently, analyses of quantitative imaging data commonly focus on summary statistics of whole tumor regions of interest (ROIs), such as the average or median tumor value of an individual imaging metric. By summarizing the tumor ROI with a single summary statistic, potentially valuable information regarding the heterogeneity of the tumor is discarded [7,47].

In this contribution, we utilize quantitative DCE-MRI and ^{18}F-FMISO-PET imaging of a murine model of HER2+ breast cancer to evaluate longitudinal alterations of intratumoral cellular and vascular in response to trastuzumab therapy. Quantitative metrics derived from these imaging strategies directly relate to the biology of the imaged tissue, allowing for the longitudinal evaluation of physiological tumor heterogeneity. While trastuzumab has been shown to alter vasculature and improve therapeutic delivery [18–20,48], longitudinal alterations in whole tumor heterogeneity have not been characterized. We employ histogram analysis of physiological parameters derived from the quantitative imaging data to characterize heterogeneity of the tumor microenvironment and correlate these findings with the gold standard of immunohistochemistry analysis. We hypothesize that quantitatively characterizing the entire tumor (instead of summarizing the cellular and vascular status with a single number) will provide increased biological information enabling a more precise separation of treatment groups.

Materials and Methods

Cell Culture and Animal Model

BT474 cells, a HER2+ human breast cancer cell line (ATCC, Manassas, VA) with an established positive response to trastuzumab [48,49], were cultured in improved minimal essential medium (Invitrogen, Carlsbad, CA) with 10% fetal bovine serum and 1% insulin at 37°C with 5% CO_2. Data from two independent cohorts of mice as part of previous studies were used in this study: one cohort from previous MRI studies [19,40] and one from a previous PET imaging study [18]. Female nude athymic mice (Charles River Laboratories, Raleigh, NC) were implanted subcutaneously with a 0.72-mg, 60-day release, 17β-estradiol pellet (Innovative Research of America, Sarasota, FL). Approximately 24 hours after 17β-estradiol implant, 10^7 BT474 breast cancer cells in serum-free media and 20% growth factor–reduced Matrigel were injected subcutaneously into the flank of the mouse. Tumors were allowed to grow until they reached ~225 mm^3 (4-6 weeks after inoculation). Mice were randomly assigned to trastuzumab-treated (10 mg/kg) or saline control groups. Intraperitoneal injections of trastuzumab or saline were given on days 0 (baseline) and 3.

Magnetic Resonance Imaging

While details are provided in previous studies [18,19,40], we briefly summarize the MRI procedure. One cohort of mice (N = 20) was imaged using a 7-T small-animal MRI scanner [Agilent Technologies (formally Varian), Palo Alto, CA] to obtain DCE-MRI on days 0, 1, and 4 (Figure 1). Two days prior to baseline imaging, mice were implanted with a jugular catheter for exogenous delivery of the MRI contrast agent. DCE-MRI acquisition parameters

were as follows: transaxial slices, 64 × 64 matrix, 1 mm slice thickness, 28 × 28 × 15 mm^3 field of view. A multislice inversion recovery snapshot fast low angle shot gradient echo sequence was used to obtain precontrast T_1 maps using seven inversion times ranging from 250 to 10,000 milliseconds. Dynamic T_1-weighted images were acquired using a spoiled gradient echo sequence with a temporal resolution of 12.8 seconds for 20 minutes. Precontrast images were collected for 2 minutes prior to the administration of 0.05 mmol/kg gadolinium-diethylenetriaminepentaacetic acid (Magnevist, Bayer, Whippany, NJ) through an automated syringe pump. For each mouse at each imaging time point, a high-resolution T_2-weighted anatomical image was utilized to manually draw ROIs around the tumor boundary for all slices containing tumor (Supplementary Figure 1).

Using a population-derived [50] arterial input function [50,51], DCE-MRI data within the tumor ROI were fit (MATLAB, Natick, MA) to the standard Kety-Tofts model [52,53] [Equation (1)] to extract parametric maps of the volume transfer coefficient (K^{trans}) and the extravascular extracellular volume fraction (v_e):

$$C_t(t) = K^{\text{trans}} \int_0^t C(u) \cdot \exp\left(-\left(K^{\text{trans}}/v_e\right)(t-u)\right) du. \quad (1)$$

Voxels which yielded nonphysiological values (e.g., $K^{trans} < 0\ min^{-1}$, $K^{trans} > 5\ min^{-1}$, $v_e < 0$, $v_e > 1$) from the DCE-MRI fitting routine were removed from subsequent analysis. The average (and 95% confidence interval) percent of tumor voxels removed was 16.5% (2.5%).

Positron Emission Tomography

While details are provided in a previous study [18], we briefly summarize the PET procedure. One cohort of mice ($N = 10$) was imaged with ^{18}F-FMISO-PET on days 0, 1, 3, 4, and 7 (Figure 1). At each imaging time point, mice were injected with approximately 350 μCi of ^{18}F-FMISO *via* retro-orbital injection prior to PET/CT imaging. After 70 minutes, a high-resolution CT scan was acquired for anatomical localization. To quantify volumetric uptake of ^{18}F-FMISO, list-mode data were collected at 90 minutes postinjection. Images were reconstructed into transaxial slices (128 × 128 × 95) with voxel sizes of 0.95 × 0.95 × 0.8 mm^3. For each voxel, the standardized uptake value (SUV) was calculated (MATLAB) using Equation (2):

$$\text{SUV} = \frac{C_{\text{img}}}{\text{ID/BW}}, \quad (2)$$

where C_{img} is the average activity concentration in the voxel, ID is the injected dose, and BW is the animal body weight in grams. For each mouse at each imaging time point, PET/CT overlays were utilized to manually draw ROIs around the tumor boundary for all slices containing tumor (Supplementary Figure 1).

Histogram and Statistical Analysis

Longitudinal alterations in heterogeneity were assessed using voxel-based frequency histogram analysis of imaging parameters in R (https://www.r-project.org/, RStudio). Group frequency histograms for K^{trans}, v_e, and SUV were generated by averaging individual mouse distributions across each treatment group at each imaging time point. Differences between parameter distributions were quantified using the two-sample Kolmogorov-Smirnov (K-S) statistic, a distance measure between each sample pair's empirical distribution functions. The K-S distance is a measure of distribution similarity ranging from 0 to 1, with a value closer to 0 representing more similar distributions and a value closer to 1 representing more different distributions; however, it is important to note that the K-S distance between distributions does not indicate the direction of change between distributions. The K-S statistic was calculated between the parameter distributions obtained at baseline and subsequent imaging time points for each individual mouse to quantify longitudinal alterations in intratumoral heterogeneity. The distance between parameter distributions were compared between treatment groups using the nonparametric Wilcoxon rank sum test. A P value of less than .05 was considered significant.

Immunohistochemistry

On the final imaging time point (i.e., day 4 for MRI and day 7 for PET), each animal was sacrificed and the tumor excised for histology. For the ^{18}F-FMISO-PET cohort of mice, 1 hour prior to sacrifice, animals were intravenously injected with pimonidazole (Hypoxyprobe, Burlington, MA). After tumor excision, tumors were sectioned

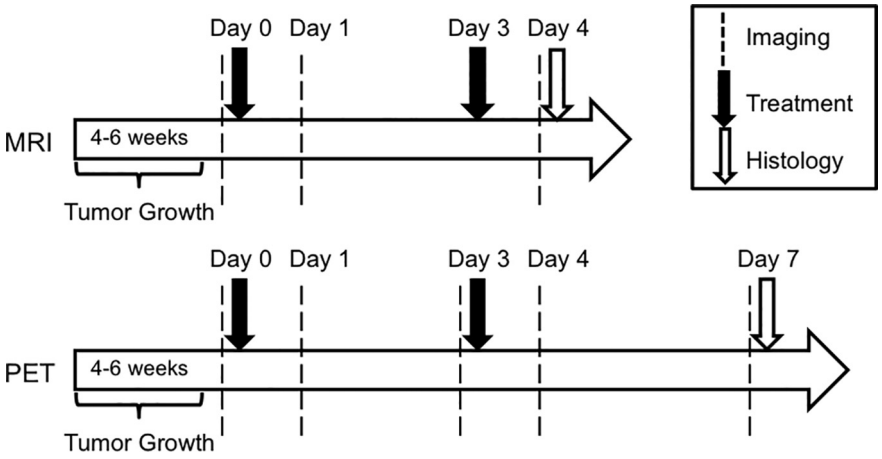

Figure 1. Schedule of tumor implantation, imaging, and treatment schedule for separate MRI and PET study cohorts. During the MRI study, tumors are imaged at day 0, 1, and 4, while during the PET study, tumors are imaged at day 0, 1, 3, 4, and 7.

at the largest cross section corresponding to the *in vivo* imaging plane and fixed in 10% formalin for 48 hours. The tissue was then stored in 70% ethanol for 72 hours, processed, and embedded in paraffin. Slices were sectioned at 5-μm thickness and floated onto charged slides and dried overnight. For each tumor, tissue sections were stained with hemotoxylin and eosin (H&E), anti-CD31 (DAKO, Carpinteria, CA), anti-Ki67 (DAKO, Carpinteria, CA), or anti-pimonidazole (Hypoxyprobe, Burlington, MA). Slides were digitally scanned in high-resolution (20×) brightfield with a Leica SCN400 (Leica Biosystems, Nussloch, Germany) slide scanner. Images were processed using Bio-Formats [54] (http://openmicroscopy.org) and MATLAB software.

For quantifying heterogeneity from immunohistochemistry data, a square tessellation technique was used derived from the work by Maley et al. [55]. Automated segmentation of histological sections stained with H&E or anti-Ki67 generated masks for individual nuclei across the entire tumor slice (Supplementary Figure 2). Automated segmentation of H&E data involved converting images to CIELAB color space and then using a *k*-means clustering algorithm to segment out nuclei. Automated segmentation of anti-Ki67 data involved converting images to HSV color space and then using Otsu thresholding to segment Ki-67+ nuclei. Automated segmentation of anti-CD31 and anti-pimonidazole data (Supplementary Figure 2) involved converting images to HSV color space and then using Otsu thresholding to segment stained areas across the entire tumor slice.

To then analyze cellular density across the tissue slice, the segmented image was divided into blocks of 150 μm × 150 μm, and individual connected components were counted within each block to yield a heat map of nuclei counts (Supplementary Figure 3). To analyze heterogeneity of vascularity or hypoxia across the tissue, the anti-CD31 or antipimonidazole segmented image, respectively, was similarly divided into blocks, and percent stain-positive area was

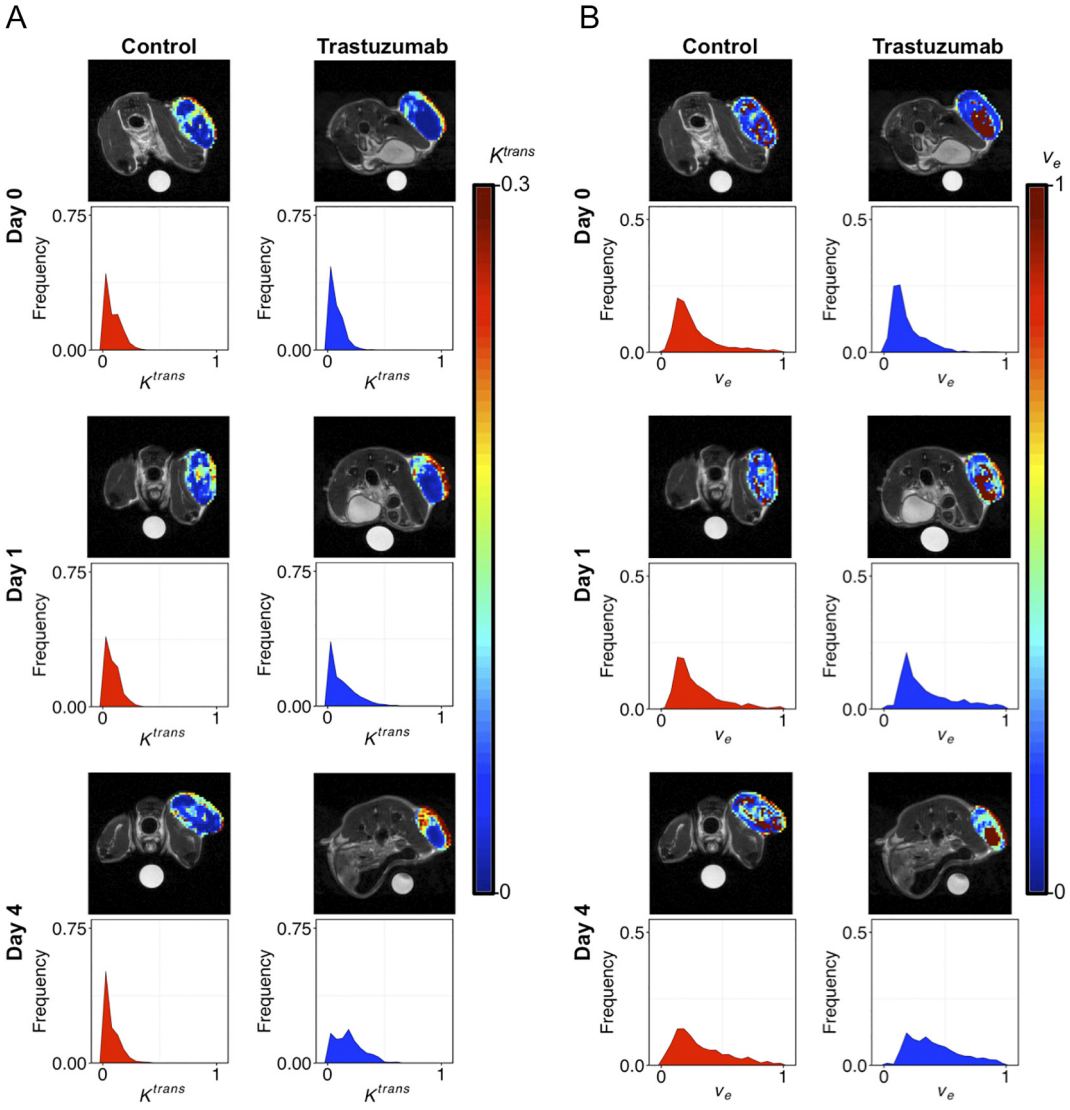

Figure 2. Representative longitudinal (progressive) control and treated animal parametric maps and voxel frequency distributions derived from DCE-MRI (K^{trans} and v_e) over 4 days. One representative animal from each treatment group is displayed in each column, while each row represents a separate time point showing a single slice of the MR image along with the associated whole tumor ROI parameter voxel distributions for that time point. The trastuzumab (TRA)-treated mouse shows a longitudinal increase in vascular heterogeneity, as measured by the K^{trans} distribution (A). The TRA-treated mouse additionally shows increased heterogeneity in cellularity, as measured by the v_e distribution (B).

quantified within each block. The interquartile range (IQR) was calculated for each resulting distribution of heat map blocks, excluding nontissue areas from analysis. The nonparametric Wilcoxon rank sum test was used to assess differences between treatment groups, with a P value less than .05 considered significant.

Correlations Between Quantitative Imaging and Histology Heterogeneity

To biologically validate quantitative imaging measures of intratumoral heterogeneity, individual mouse parameter distributions were correlated to corresponding histology data. Parameter distributions of the tumor ROI within the central slice at the study end point (day 4 for MRI, day 7 for PET) imaging data were used to calculate IQR values for each individual mouse parameter distribution. IQR values for distributions of heat map blocks from histology data were correlated with IQR values for parameter distributions of the matching central slice from quantitative imaging data. Comparisons of heterogeneity were made for the following: CD31 vessel area and K^{trans}, H&E nuclei count and v_e, and pimonidazole percent stained area and SUV. Correlations were tested using Pearson's product-moment correlation, and a P value less than .05 was considered significant.

Results

Histogram Analysis of Quantitative DCE-MRI

Figure 2 shows representative control and trastuzumab-treated K^{trans} and v_e parameter maps derived from DCE-MRI data. Quantitative analysis of K^{trans} distributions showed a longitudinal increase in vascular heterogeneity upon trastuzumab treatment (Figure 3*A*). Figure 3, *B-C* shows box and whisker plots of K-S distance measures for each individual mouse between baseline and day 1 (Figure 3*B*), and baseline and day 4 (Figure 3*C*) K^{trans} distributions. On day 1, there were no significant differences in K^{trans} distributions between control and treated groups, with a mean K-S distance from baseline of 0.23 for both treatment groups (P = .53, Figure 3*B*), indicating no change in vascular heterogeneity. On day 4, individual control K^{trans} distributions showed little change in vascular heterogeneity from baseline, with a mean K-S distance of 0.21 (Figure 3*C*). Trastuzumab-treated mice, however, revealed a longitudinal increase in vascular heterogeneity on day 4, as indicated by the increase in the tails of the grouped distribution (Figure 3*A*). Furthermore, K^{trans} distributions in the trastuzumab-treated cohort showed an increased mean K-S distance of 0.42 on day 4 (P < .01, Figure 3*C*), demonstrating increased vascular heterogeneity.

Quantitative analysis of v_e distributions showed a longitudinal increase in cellularity heterogeneity upon trastuzumab treatment (Figure 4*A*). Figure 4, *B* and *C* show box and whisker plots of K-S distance measures for each individual mouse between baseline and day 1 (Figure 4*B*), and baseline and day 4 (Figure 4*C*) v_e distributions. On day 1, there were no significant differences in v_e distributions between control and treated groups, with a mean K-S distance from baseline of 0.18 and 0.22, respectively (P = .44, Figure 4*B*), indicating no change in cellularity heterogeneity. On day 4, individual control v_e distributions showed little change in cellularity heterogeneity from baseline, with a mean K-S distance of 0.22 (Figure 4*C*).

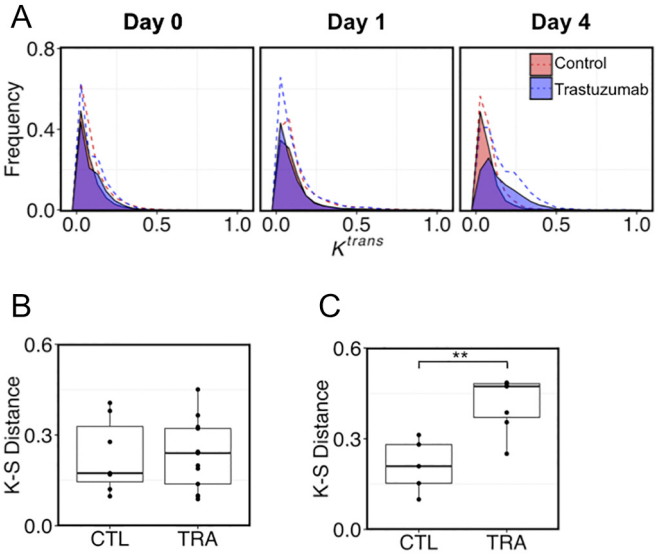

Figure 3. Alterations in K^{trans} distributions for treatment groups over time. Panel A shows average K^{trans} distributions for each treatment group over time, with dashed lines representing the standard deviation. Panels B and C display box and whisker plots of K-S distances between baseline and day 1 (B) and baseline and day 4 (C) for the K^{trans} distributions for each individual mouse from the control (CTL) and trastuzumab (TRA) -treated groups. Individual mouse K-S distances are shown as points overlaid on each box and whisker plot (B and C). The K^{trans} distributions for TRA-treated tumors show a longitudinal increase in vascular heterogeneity with increased frequency in the distribution tail (A), as well as an increased mean K-S distance of 0.42 compared to CTL mean K-S distance of 0.21 (**P < .01, C).

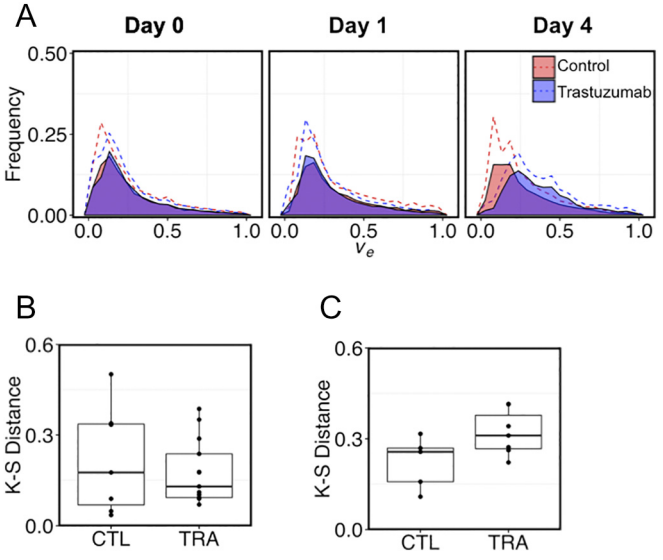

Figure 4. Alterations in v_e frequency distributions for treatment groups over time. Panel A shows average frequency v_e distributions for each treatment group over time, with dashed lines representing the standard deviation. Panels B and C display box and whisker plots of K-S distances between baseline and day 1 (B), and baseline and day 4 (C) for the v_e distributions for each individual mouse from the CTL and TRA-treated groups. Individual mouse K-S distances are shown as points overlaid on each box and whisker plot (B-C). The v_e distributions for the TRA-treated tumors show a longitudinal increase in cellular heterogeneity with increased frequency in the distribution tail (A), as well as an increased mean K-S distance of 0.32 compared to a CTL mean K-S distance of 0.22 (P = .05, not significant, C).

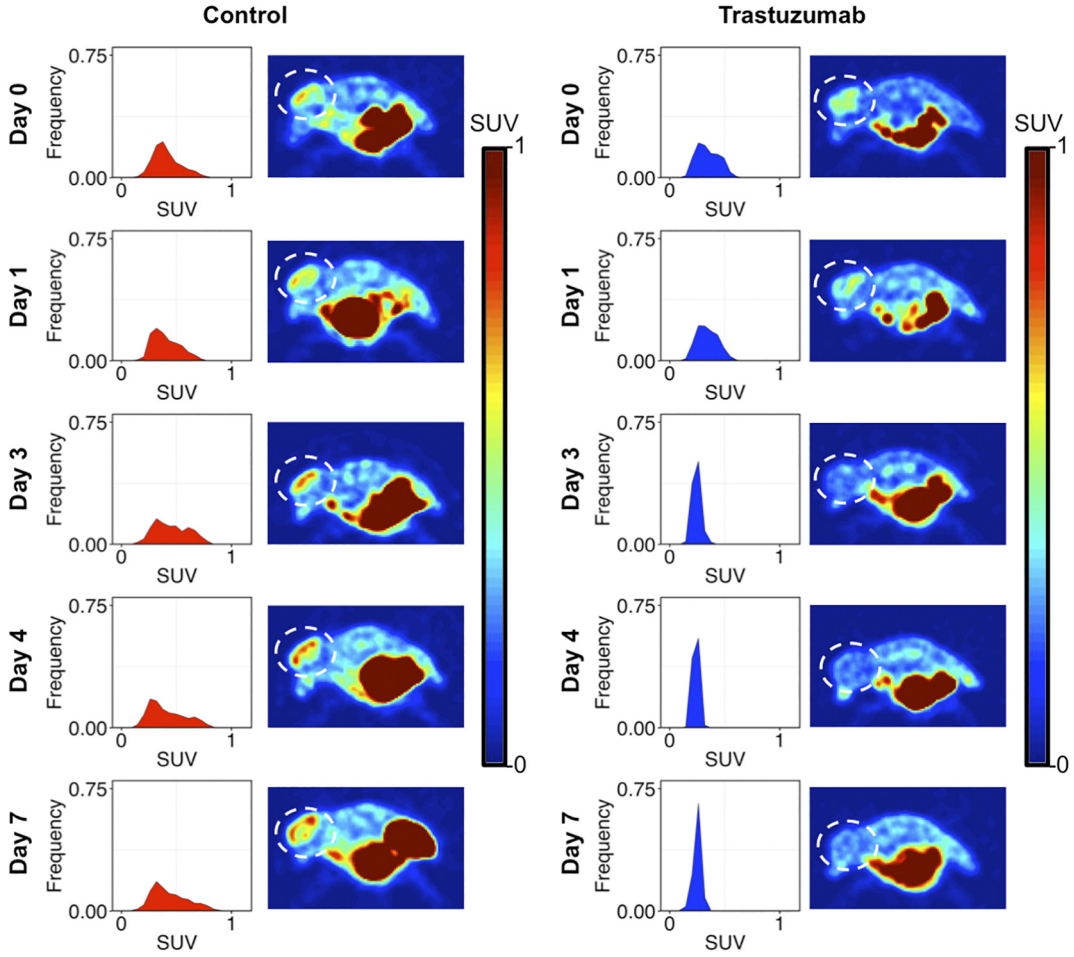

Figure 5. Representative longitudinal CTL and treated ^{18}F-FMISO-PET images and SUV frequency distributions over 7 days. One representative animal of each treatment group is displayed in each column, while each row represents a separate time point showing a single slice of the PET image (tumor denoted by dashed circle) along with the associated whole tumor ROI SUV voxel distributions for that time point. The example TRA-treated mouse (right column) shows a decrease in hypoxic heterogeneity over time.

Trastuzumab-treated mice, however, showed a longitudinal increase in cellularity heterogeneity on day 4, as observed by the increase in the tails of the grouped distribution (Figure 4*A*). Furthermore, v_e distributions for the trastuzumab-treated cohort showed an increased mean K-S distance of 0.32 on day 4 (P = .05), demonstrating increased cellularity heterogeneity.

Histogram Analysis of Quantitative ^{18}F-FMISO-PET

Representative control and trastuzumab-treated *SUV* images are shown in Figure 5. Quantitative analysis of *SUV* distributions showed longitudinal decrease in heterogeneity of oxygen distribution upon trastuzumab treatment (Figure 6*A*). Figure 6, *B-E* shows box and whisker plots of K-S distance measures for each individual mouse between baseline and day 1 (Figure 6*B*), day 3 (Figure 6*C*), day 4 (Figure 6*D*), and day 7 (Figure 6*E*) *SUV* distributions. On day 1, there were no significant differences in *SUV* distributions between control and treated groups, with a mean K-S distance from baseline of 0.18 and 0.12, respectively (P = .79, Figure 6*B*), indicating no change in hypoxia heterogeneity. On day 3, individual control *SUV* distributions showed little change in heterogeneity of oxygenation from baseline with a mean K-S distance of 0.12 (Figure 6*C*). Trastuzumab-treated mice, however, revealed a longitudinal decrease in hypoxia heterogeneity on day 3, with a narrowing of the treated *SUV* distribution (Figure 6*A*). Additionally, individual treated mouse *SUV* distributions showed an increased mean K-S distance of 0.42 on day 3 (P = .05), demonstrating decreased heterogeneity of oxygenation across the tumor. By day 7, control mice demonstrated a longitudinal increase in hypoxic heterogeneity, with a widening of *SUV* distributions (Figure 6*A*) and an increased mean K-S distance of 0.28 from the baseline distribution (Figure 6*E*). Conversely, on day 7, trastuzumab-treated mice showed a longitudinal decrease in hypoxic heterogeneity, with a narrowing of *SUV* distributions (Figure 6*A*) and an increased mean K-S distance of 0.46 from the baseline distribution (P = .047, Figure 6*E*).

Histogram Analysis of Immunohistochemistry Data

Figure 7 shows representative mouse histological sections acquired on day 4 (corresponding to the end point of the DCE-MRI study) stained with H&E, anti-CD31, or anti-Ki67 to measure cellular density, vessel area, and proliferating cellular density, respectively. Example mouse sections from each treatment group are shown in Figure 7, *A-C*, alongside associated heat maps and kernel density estimates of heat map distributions. Figure 7*D* displays box and whisker plots of IQR values for each stain's heat map distribution across treatment groups. Treatment cohort distributions are visualized in Supplementary Figure 4, *A-B*. On day 4, no statistically significant difference was observed between the trastuzumab-treated and control groups for H&E nuclei count

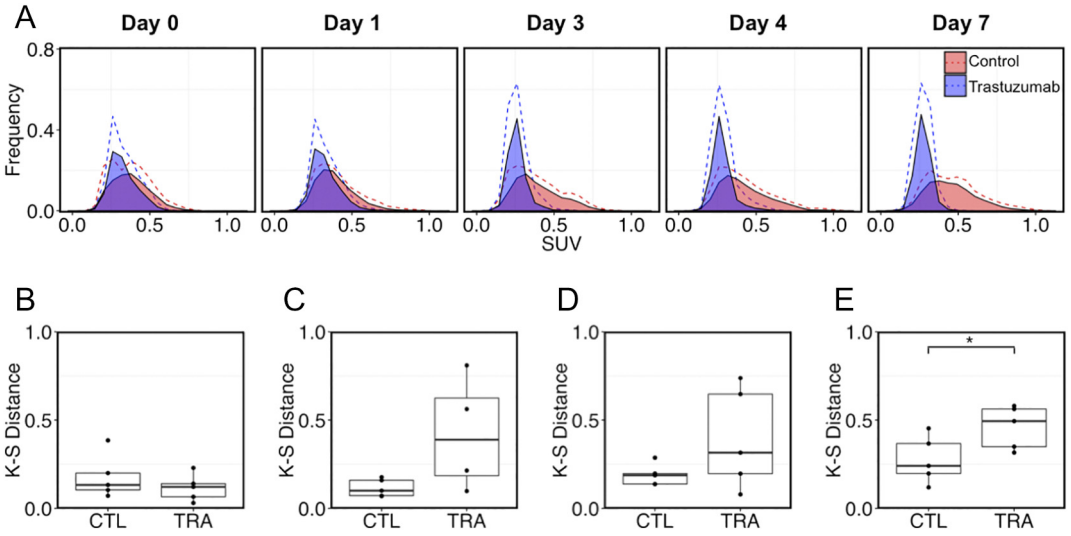

Figure 6. Alterations in SUV frequency distributions for treatment groups over time. Panel A shows average frequency SUV distributions for each treatment group over time, with dashed lines representing the standard deviation. Box and whisker plots of K-S distances between baseline and day 1 (B), day 3 (C), day 4 (D), and day 7 (E) for the SUV distributions are shown for each individual mouse from the CTL CTL and TRA-treated groups. Individual mouse K-S distances are shown as points overlaid on each box and whisker plot (B-E). The SUV distributions from CTL tumors show a longitudinal increase in hypoxia heterogeneity with an increased voxel frequency in the distribution tail (A) and a K-S distance of 0.28 from baseline, at day 7 (E). Conversely, SUV distributions for the TRA-treated tumors show a longitudinal decrease in hypoxia heterogeneity with a narrowing of the distribution (A) and a K-S distance of 0.46 from baseline at day 7 (*P = .047, E).

distributions (mean treated IQR = 87.83, control IQR = 70.75, P = .57, Figure 7*D*), CD31 percent vessel area distributions (mean treated IQR = 1.59 control IQR = 1.42, P = .87, Figure 7*D*), or Ki67+ nuclei count distributions (mean treated IQR = 19.25, control IQR = 23.50, P = .57, Figure 7*D*).

Figure 8 shows representative mouse histological sections acquired on day 7 (corresponding to the end point of the ^{18}F-FMISO-PET study) stained with H&E, anti-CD31, and antipimonidazole to measure cellular density, vessel area, and hypoxia, respectively. Example mouse sections from each treatment group are shown in Figure 8, *A-C*, alongside associated heat maps and kernel density estimates of heat map distributions. Figure 8*D* displays box and whisker plots of IQR values for each stain's heat map distribution across treatment groups. Treatment cohort distributions are visualized in Supplementary Figure 4, *C-D*. On day 7, no statistically significant difference was observed between the trastuzumab-treated and control groups for H&E nuclei count distributions, with a mean IQR of 84.5 and 114.0, respectively (P = .21, Figure 8*D*). Trastuzumab-treated tumors had increased vascular heterogeneity, with CD31 percent vessel area distributions showing a mean IQR of 1.72 compared to control mean IQR of .95 (P = .02, Figure 8*D*). Additionally, trastuzumab-treated tumors had decreased hypoxia heterogeneity, with pimonidazole percent area distributions showing a mean IQR of 0, compared to control mean IQR of 8.05 (P < .01, Figure 8*D*).

Correlations Between Imaging and Histology Heterogeneity

Figure 9*B* shows a positive linear correlation between CD31 percent stained area heterogeneity (vessel percent area IQR) and quantitative imaging measures of vascular heterogeneity (K^{trans} IQR) with an r^2 = 0.33 (P = .05). No correlation was observed between v_e and H&E nuclei counts (Figure 9*C*). Figure 9*D* shows a positive linear correlation between pimonidazole percent stained area heterogeneity and quantitative imaging measures of hypoxia heterogeneity (SUV IQR) with an r^2 = 0.69 (P < .01).

Discussion

In this work, we demonstrated that measures of tumor microenvironment heterogeneity, derived from quantitative imaging, and their longitudinal alterations can be used to distinguish treatment response in a preclinical model of HER2+ breast cancer. Histogram analysis of DCE-MRI derived parametric maps revealed increased heterogeneity in cellularity upon trastuzumab treatment, with a widening of the v_e distribution for treated mice longitudinally, and compared to control tumors. The treated group showed increased spread of the v_e distribution, and this longitudinal increase in cellularity heterogeneity across trastuzumab tumors is expected with increased cell death. Histogram analysis of K^{trans} parametric maps showed increased vascular heterogeneity with trastuzumab treatment with a spreading of treated mice K^{trans} distributions over time and compared to control mice. Although a positive correlation is observed between CD31-stained vessel density and K^{trans} heterogeneity, immunohistochemistry analysis of vascular heterogeneity on day 4 showed no difference in CD31-stained vessel density between treatment and control. This is not surprising since K^{trans} is a mixed measure of vessel permeability and perfusion; while vessel density may be similar between treatment and control groups, vascular delivery is not solely a function of vessel density. Trastuzumab therapy revealed improved oxygenation across the tumor with a narrowing of ^{18}F-FMISO-PET *SUV* distributions over time and compared to control mice. Pimonidazole staining of excised tissue from day 7 validated the observed decrease in hypoxic heterogeneity of the treated mice; in particular, there was a decrease in the mean IQR of distributions of pimonidazole percent area for treated mice compared to the control mice. These results are consistent with ^{18}F-FMISO-PET results of decreased hypoxic

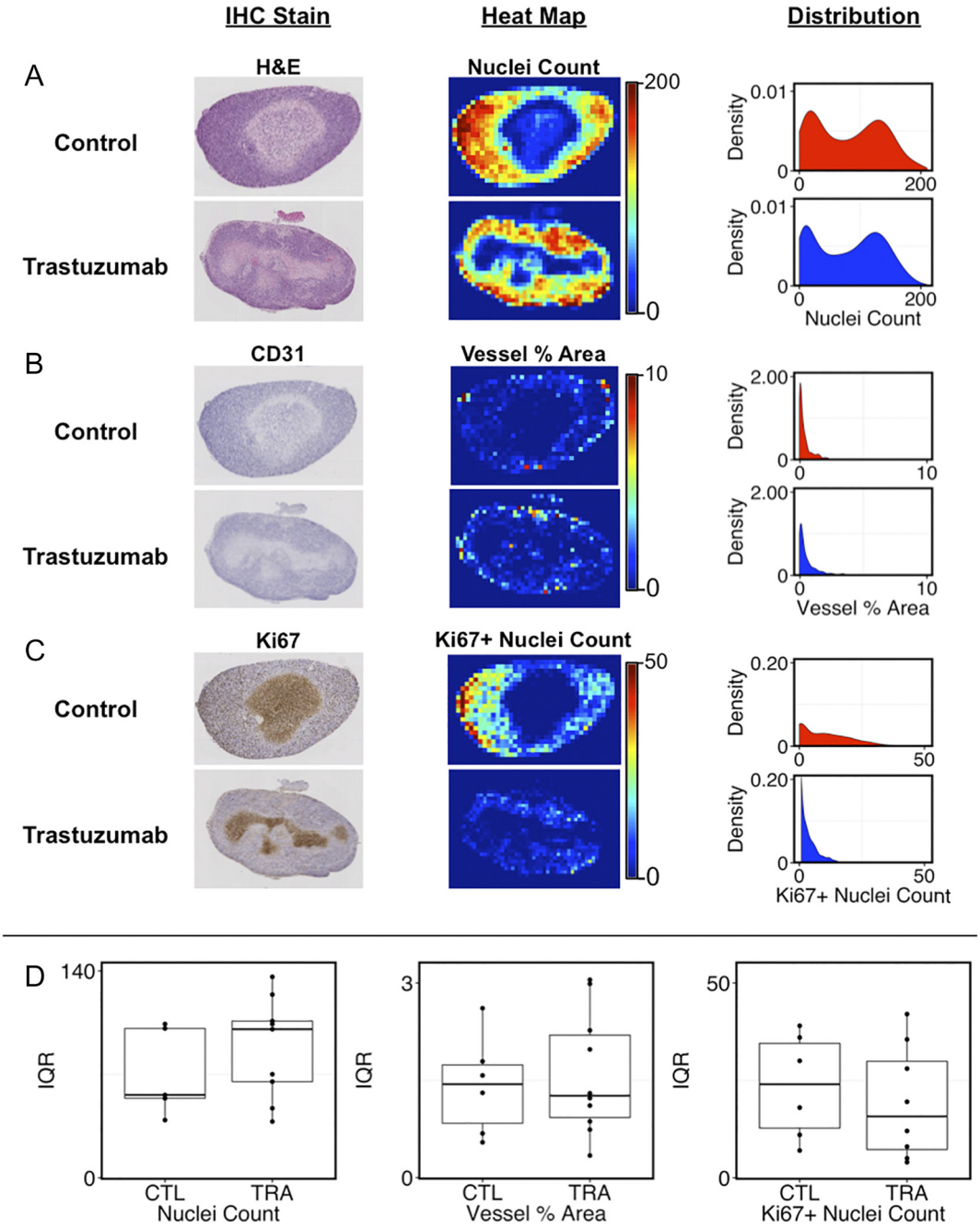

Figure 7. Representative histology from MRI study end point. From the MRI study end point (day 4), representative CTL and treated animal histology sections, associated heat maps, and distributions are shown for (A) H&E-stained nuclei, (B) anti-CD31 vessel area, and (C) anti-Ki67 positive nuclei. Each row in panels A-C shows a representative animal from each treatment group. The first column (IHC Stain) for panels A-C shows representative animal histology sections. The second and third columns for panels A-C show the corresponding representative heat maps and associated distributions, respectively, for (A) cellularity, (B) vessel percent area, and (C) Ki67+ proliferating cellularity. The representative CTL and TRA mice show similar cellularity and vascular heterogeneity (A-B). However, the TRA-treated mouse shows decreased levels of proliferating cellularity (C). These trends held similarly across the treatment cohorts, as seen in panel D, showing IQR values for heat map distributions of each mouse. No statistically significant differences in mean IQR values were observed between the treatment groups.

heterogeneity observed *in vivo*. CD31 staining on day 7 was also in agreement with ^{18}F-FMISO-PET results, having shown an increase in vessel density across the tumor, corresponding with increased vascular heterogeneity upon trastuzumab treatment. Our study showed quantitative imaging-derived measures of tumor microenvironment heterogeneity were consistent with immunohistochemical measures of microenvironment heterogeneity and able to distinguish treatment response in a preclinical model of HER2+ breast cancer.

Our study utilized voxel-based histogram analysis of quantitative imaging data and showed that trastuzumab treatment improved vascular delivery and alleviated hypoxia, resulting in more

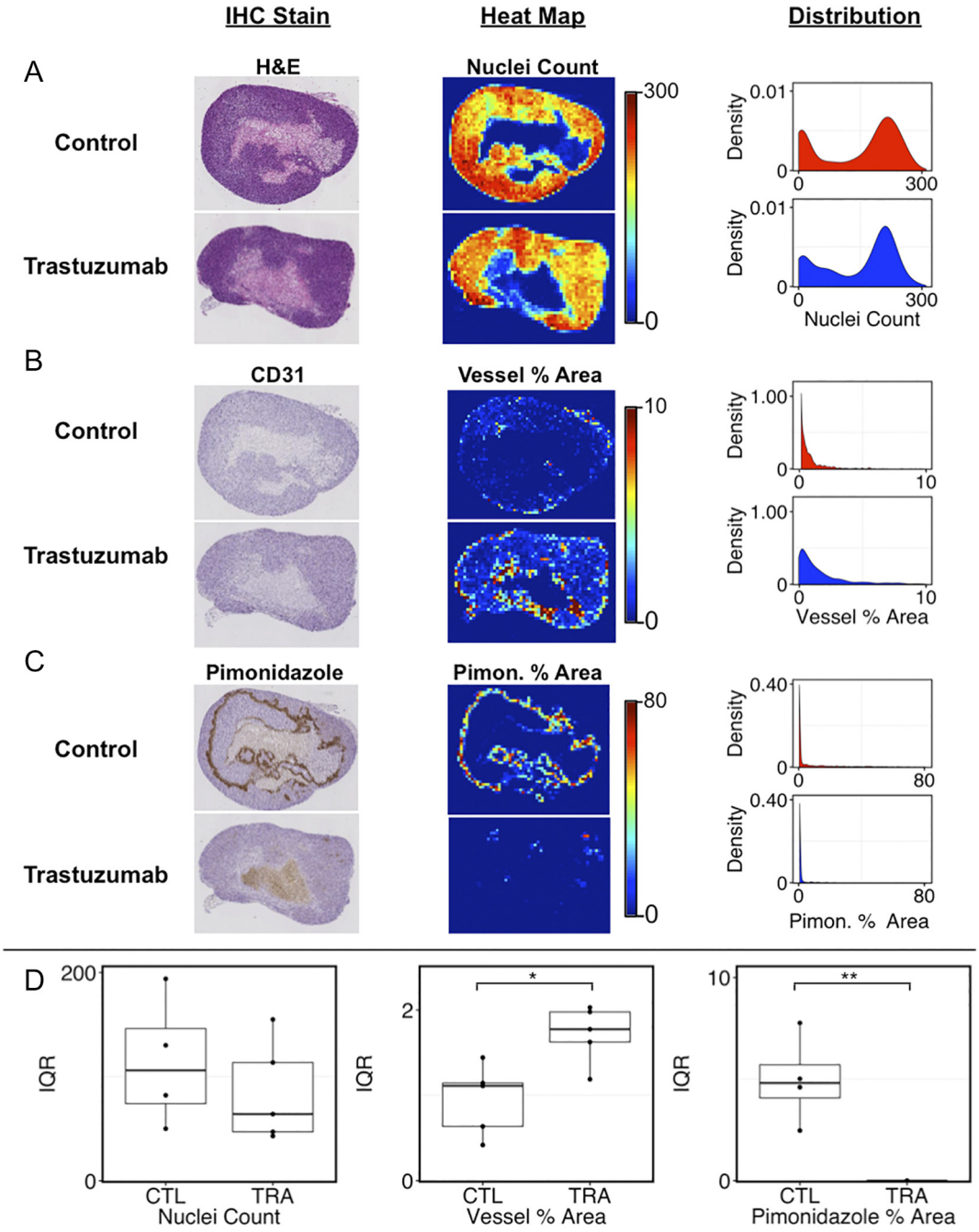

Figure 8. Representative histology from PET study end point. Representative CTL and treated histology sections and the associated heat maps and distributions are shown for (A) H&E-stained nuclei, (B) anti-CD31 vessel area, and (C) antipimonidazole-stained area are shown from the PET study end point (day 7). Each row in panels A-C shows a representative animal from each treatment group. The first column for panels A-C shows representative histology sections (column labeled IHC stains). The second and third columns for panels A-C show corresponding representative heat maps and the associated distributions, respectively, for (A) cellularity, (B) vessel percent area, and (C) pimonidazole percent area. The representative CTL and TRA mice show similar cellularity heterogeneity (A). However, the TRA-treated mouse shows increased vascular heterogeneity (B) and decreased levels of hypoxia (C). These trends held similarly across the treatment cohorts, as seen in panel D, showing IQR values for heat map distributions for each mouse. The TRA-treated cohort shows increased vascular heterogeneity with vessel percent area distributions having a mean IQR of 1.72 compared to the CTL IQR of 0.95 (*$P = .02$, D). Furthermore, the TRA-treated cohort shows decreased hypoxic heterogeneity with pimonidazole percent area distributions having a mean IQR of 0 compared to the CTL mean IQR of 8.05 (**$P < .01$, D).

homogenous oxygenation across the tumor ROI. As it is widely known that tumors are spatially heterogeneous, summarizing an entire tumor with a single mean parameter value potentially eliminates a great deal of critical information. Histogram analysis of imaging data enables the quantitative characterization of that heterogeneity across the tumor volume that would be lost when only summary statistics are employed. While characterization of intratumoral heterogeneity using histogram analysis is not uncommon, histogram analysis of quantitative imaging data typically involves a bin-wise comparison of the test group's average histograms

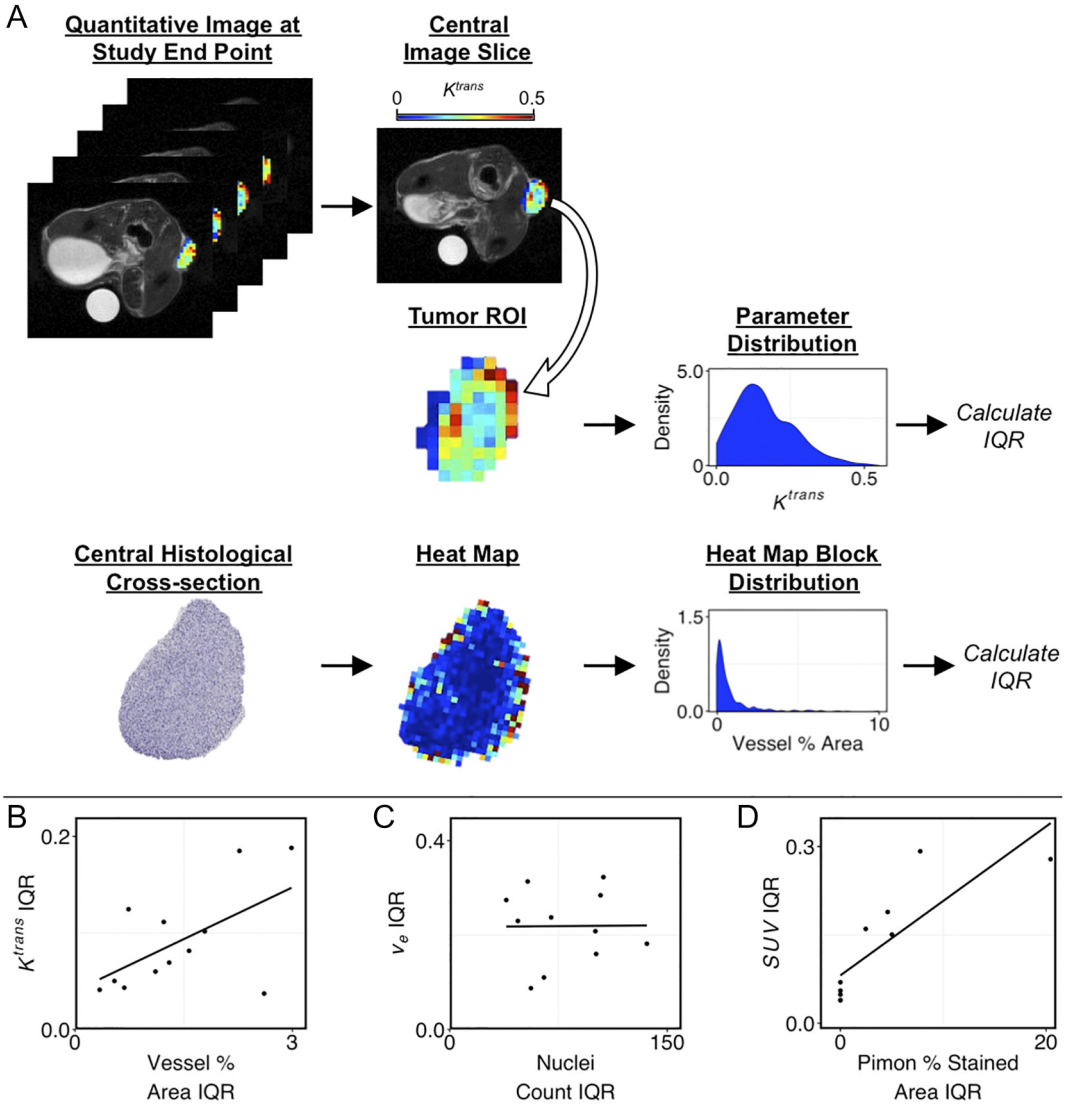

Figure 9. Correlation of quantitative imaging distributions to histological distributions at the study end point. Central imaging slices were selected from study end point MRI and PET data (A). IQR values were calculated for quantitative imaging parameter distributions for each mouse tumor ROI. IQR values were also calculated for heat map block distributions from individual mouse histology data. The correlation was calculated between IQR values of the following distributions: vessel percent area and K^{trans} (B), nuclei count and v_e (C), and pimonidazole percent stained area and SUV (D). Quantitative imaging of vascular permeability and perfusion (K^{trans}) showed a positive linear correlation with vessel percent area (B, $r^2 = 0.33$, $P = .05$). No correlation was observed between v_e and nuclei counts (C). Quantitative imaging of hypoxia (SUV) showed a positive linear correlation with pimonidazole percent stained area (D, $r^2 = 0.69$, $P < .01$).

compared to that of the control [29]. Crokart et al. utilized this approach to histogram analysis of DCE-MRI parameter distributions to assess differences in perfusion characteristics between control and NSAID-treated tumors [56]. Additionally, Li et al. investigated histogram analysis of DCE-MRI derived parametric maps to evaluate heterogeneity of response to antiangiogenic therapy [57]. Comparatively, our work utilizes the K-S distance to measure differences of each mouse's parameter distribution posttreatment from its distribution at baseline, thereby personalizing the approach by comparing changes in heterogeneity at the individual tumor level.

Our observations of increased vascular heterogeneity upon trastuzumab treatment are further supported by other studies which have shown alterations in tumor vasculature and oxygenation in preclinical models of HER2+ cancer in response to trastuzumab therapy [20,58–61]. In a HER2+ murine model of brain cancer, Izumi et al. utilized optical imaging to show significant decrease in vascular permeability in response to trastuzumab therapy along with increased rates of survival [20]. Using hyperspectral imaging, with CD31 IHC staining for validation, McCormack et al. observed increased vessel density in HER2+ BT474 tumors upon trastuzumab treatment [58]. Furthermore, Hardee et al. utilized a transfected MCF7 cell line, constitutively expressing HER2, to demonstrate decreased hypoxia, as quantified by pimonidazole staining, in trastuzumab-treated MCF7-^{Her2} tumors compared to untreated MCF7^{WT} controls [60].

In an effort to combat treatment challenges posed by intratumoral heterogeneity, recent work has investigated methods to alter the tumor microenvironment and reduce vascular heterogeneity in the hopes of yielding more treatment sensitive tumors [62–64]. Here we demonstrated that trastuzumab therapy increased cellular and vascular heterogeneity and reduced heterogeneity in tumor

oxygenation across the tumor. In previous work with the same murine model of HER2+ breast cancer, we have shown that sequential delivery of trastuzumab prior to half the standard dose of the cytotoxic therapy, doxorubicin, was as effective at reducing tumor volume as simultaneous delivery of trastuzumab and a full dose of doxorubicin [19]. These results taken together demonstrate the ability of trastuzumab to improve vascular delivery of cytotoxic therapy across the tumor. Furthermore, these results highlight the importance of longitudinal analysis of tumor microenvironment heterogeneity because with improved therapeutic delivery, cytotoxic drug dose and associated harmful side effects can be reduced.

One limitation of our study is the lack of biological validation at each imaging time point. Tumors were only excised at the end point of the quantitative imaging study; however, this was required for the longitudinal measurement of quantitative imaging parameters and analysis of tumor microenvironment heterogeneity over time. Additionally, biological validation was only performed on one to two cross-sectional slices of the excised tumor for each immunohistochemistry stain. While the entire tumor slice was quantitatively evaluated, the central slice is only representative of a small portion of the tumor. Future work will involve biological validation using the whole tumor and comparing biological heterogeneity measures to those observed with quantitative imaging. Another limitation of our study is the one-dimensional assessment of intratumoral heterogeneity through histogram analysis of quantitative imaging parameter maps. Most analyses of quantitative imaging data involve averaging across the tumor ROI, forgoing much of the information about physiological heterogeneity across the tumor. While we address this shortcoming utilizing voxel-based histogram analysis of quantitative imaging data, we do lose information regarding spatial heterogeneity. Future work will involve developing methodologies to analyze tumor microenvironment heterogeneity in 3D across the imaged tumor. Additionally, alternative techniques involving MR oximetry (e.g., oxygen-enhanced MRI or tissue oxygen level–dependent MRI) may provide the opportunity to collect similar oxygen data as ^{18}F-FMISO-PET without the necessity of an exogenous, radioactive tracer [65], which is important for future clinical translation. Furthermore, this could allow for both oxygen and vascular (DCE-MRI) data from one imaging session, along with combined analysis of these parameters within a spatially aligned data set.

Conclusion

We have demonstrated the value in quantifying whole tumor, voxel-wise alterations in the tumor microenvironment heterogeneity over time and in response to therapy. In particular, DCE-MRI and ^{18}F-FMISO-PET reveal quantitative longitudinal changes in the three-dimensional heterogeneity of tumor cellular, and vascular features could serve as early indicators for treatment response to help guide therapy for patients with HER2+ breast cancer.

Supplementary data to this article can be found online at https://doi.org/10.1016/j.neo.2018.10.008.

Acknowledgements

We thank the Cancer Prevention and Research Institute of Texas for support through RR160005, and the American Cancer Society for support through RSG-18-006-01-CCE. We thank the National Cancer Institute for funding through R01CA138599 and U01CA174706 and the National Institute of Biomedical Imaging and Bioengineering for support through T32 EB007507.

References

[1] Marusyk A and Polyak K (2010). Tumor heterogeneity: causes and consequences. *Biochim Biophys Acta BBA Rev Cancer* **1805**, 105–117.
[2] Greaves M and Maley CC (2012). Clonal evolution in cancer. *Nature* **481**, 306–313.
[3] Tumor Microenvironment and Cellular Stress, 772. New York: Springer; 2014 .
[4] Ward C, Langdon SP, Mullen P, Harris AL, Harrison DJ, Supuran CT, and Kunkler IH (2013). New strategies for targeting the hypoxic tumour microenvironment in breast cancer. *Cancer Treat Rev* **39**, 171–179.
[5] Junttila MR and de Sauvage FJ (2013). Influence of tumour micro-environment heterogeneity on therapeutic response. *Nature* **501**, 346–354.
[6] Goel S, Duda DG, Xu L, Munn LL, Boucher Y, Fukumura D, and Jain RK (2011). Normalization of the vasculature for treatment of cancer and other diseases. *Physiol Rev* **91**, 1071–1121.
[7] O'Connor JPB, Rose CJ, Waterton JC, Carano RAD, Parker GJM, and Jackson A (2015). Imaging intratumor heterogeneity: role in therapy response, resistance, and clinical outcome. *Clin Cancer Res* **21**, 249–257.
[8] Zardavas D, Irrthum A, Swanton C, and Piccart M (2015). Clinical management of breast cancer heterogeneity. *Nat Rev Clin Oncol* **12**, 381–394.
[9] Alizadeh AA, Aranda V, Bardelli A, Blanpain C, Bock C, Borowski C, Caldas C, Califano A, Doherty M, and Elsner M, et al (2015). Toward understanding and exploiting tumor heterogeneity. *Nat Med* **21**, 846–853.
[10] Kohler BA, Sherman RL, Howlader N, Jemal A, Ryerson AB, Henry KA, Boscoe FP, Cronin KA, Lake A, and Noone A-M, et al (2015). Annual report to the nation on the status of cancer, 1975-2011, featuring incidence of breast cancer subtypes by race/ethnicity, poverty, and state. *J Natl Cancer Inst* **107**, 1–25.
[11] Anderson WF, Rosenberg PS, and Katki HA (2014). Tracking and Evaluating Molecular Tumor Markers With Cancer Registry Data: HER2 and Breast Cancer. *J Natl Cancer Inst* **106**, 1–3.
[12] Dean-Colomb W and Esteva FJ (2008). Her2-positive breast cancer: herceptin and beyond. *Eur J Cancer* **44**, 2806–2812.
[13] Novel Biomarkers in the Continuum of Breast Cancer, 882. Springer International Publishing; 2016.
[14] Ng CK, Martelotto LG, Gauthier A, Wen H-C, Piscuoglio S, Lim RS, Cowell CF, Wilkerson PM, Wai P, and Rodrigues DN, et al (2015). Intra-tumor genetic heterogeneity and alternative driver genetic alterations in breast cancers with heterogeneous HER2 gene amplification. *Genome Biol.* **16**, 1–21.
[15] Onsum MD, Geretti E, Paragas V, Kudla AJ, Moulis SP, Luus L, Wickham TJ, McDonagh CF, MacBeath G, and Hendriks BS (2013). Single-cell quantitative HER2 measurement identifies heterogeneity and distinct subgroups within traditionally defined HER2-positive patients. *Am J Pathol* **183**, 1446–1460.
[16] Nahta R and Esteva FJ (2007). Trastuzumab: triumphs and tribulations. *Oncogene* **26**, 3637–3643.
[17] Martin-Castillo B, et al (2013). Basal/HER2 breast carcinomas: integrating molecular taxonomy with cancer stem cell dynamics to predict primary resistance to trastuzumab (Herceptin). *Cell Cycle* **12**, 225–245.
[18] Sorace AG, et al (2017). Quantitative [18F]FMISO PET imaging shows reduction of hypoxia following trastuzumab in a murine model of HER2+ breast cancer. *Mol Imaging Biol* **19**, 130–137.
[19] Sorace AG, et al (2016). Trastuzumab improves tumor perfusion and vascular delivery of cytotoxic therapy in a murine model of HER2+ breast cancer: preliminary results. *Breast Cancer Res Treat* **155**, 273–284.
[20] Izumi Yotaro, Fukumura Dai, Xu Lei, and Jain Rakesh K (2002). Herceptin acts as an anti-angiogenic cocktail. *Nature* **416**, 279.
[21] Hudis CA (2007). Trastuzumab—mechanism of action and use in clinical practice. *N Engl J Med* **357**, 39–51.
[22] Vogel CL, Cobleigh MA, Tripathy D, Gutheil JC, Harris LN, Fehrenbacher L, Slamon DJ, Murphy M, Novotny WF, and Burchmore M (2002). Efficacy and safety of trastuzumab as a single agent in first-line treatment of HER2-overexpressing metastatic breast cancer. *J Clin Oncol* **20**, 719–726.
[23] Fiszman GL and Jasnis MA (2011). Molecular mechanisms of trastuzumab resistance in her2 overexpressing breast cancer. *Int J Breast Cancer* **2011**, 1–11.
[24] Huang Y-E, Chen C-F, Huang Y-J, Konda SD, Appelbaum DE, and Pu Y (2010). Interobserver variability among measurements of the maximum and mean standardized uptake values on 18 F-FDG PET/CT and measurements of tumor size on diagnostic CT in patients with pulmonary tumors. *Acta Radiol* **51**, 782–788.

[25] Orel SG, Kay N, Reynolds C, and Sullivan DC (1999). BI-RADS categorization as a predictor of malignancy. *Radiology* **211**, 845–850.

[26] Burrell HC, Pinder SE, Wilson AR, Evans AJ, Yeoman LJ, Elston CW, and Ellis IO (1996). The positive predictive value of mammographic signs: a review of 425 non-palpable breast lesions. *Clin Radiol* **51**, 277–281.

[27] O'Connor E, Fieller N, Holmes A, and Waterton J (2005). How to analyse dynamic MRI in oncology; advanced histogram analysis gives better statistical power & insight than simple averaging. Proc Intl Soc Magn Reson Med, 13.; 2005. p. 2101.

[28] Tan S, Zhang H, Zhang Y, Chen W, D'Souza WD, and Lu W (2013). Predicting pathologic tumor response to chemoradiotherapy with histogram distances characterizing longitudinal changes in 18F-FDG uptake patterns. *Med Phys* **40**101707.

[29] Just N (2014). Improving tumour heterogeneity MRI assessment with histograms. *Br J Cancer* **111**, 2205–2213.

[30] Alic L, Niessen WJ, and Veenland JF (2014). Quantification of heterogeneity as a biomarker in tumor imaging: a systematic review. *PLoS ONE* **9**e110300.

[31] Teruel JR, Heldahl MG, Goa PE, Pickles M, Lundgren S, Bathen TF, and Gibbs P (2014). Dynamic contrast-enhanced MRI texture analysis for pretreatment prediction of clinical and pathological response to neoadjuvant chemotherapy in patients with locally advanced breast cancer. *NMR Biomed* **27**, 887–896.

[32] Nyflot MJ, Yang F, Byrd D, Bowen SR, Sandison GA, and Kinahan PE (2015). Quantitative radiomics: impact of stochastic effects on textural feature analysis implies the need for standards. *J Med Imaging* **2**, 041002.

[33] Asselin M-C, O'Connor JPB, Boellaard R, Thacker NA, and Jackson A (2012). Quantifying heterogeneity in human tumours using MRI and PET. *Eur J Cancer* **48**, 447–455.

[34] Yankeelov Thomas and Gore (2007). J. Dynamic contrast enhanced magnetic resonance imaging in oncology: theory, data acquisition, analysis, and examples. *Curr Med Imaging Rev* **3**, 91–107.

[35] Krohn KA, Link JM, and Mason RP (2008). Molecular imaging of hypoxia. *J Nucl Med* **49**, 129S–148S.

[36] Dunphy MPS and Lewis JS (2009). Radiopharmaceuticals in preclinical and clinical development for monitoring of therapy with PET. *J Nucl Med* **50**(Suppl. 1), 106S–121S.

[37] Li X, Arlinghaus LR, Ayers GD, Chakravarthy AB, Abramson RG, Abramson VG, Atuegwu N, Farley J, Mayer IA, and Kelley MC, et al (2014). DCE-MRI analysis methods for predicting the response of breast cancer to neoadjuvant chemotherapy: pilot study findings: DCE-MRI to Predict Breast Cancer Treatment Response. *Magn Reson Med* **71**, 1592–1602.

[38] Rajendran JG, Mankoff DA, O'Sullivan F, Peterson LM, Schwartz DL, Conrad EU, Spence AM, Muzi M, Farwell DG, and Krohn KA (2004). Hypoxia and glucose metabolism in malignant tumors evaluation by [18F] fluoromisonidazole and [18F] fluorodeoxyglucose positron emission tomography imaging. *Clin Cancer Res* **10**, 2245–2252.

[39] Thorwarth D and Alber M (2010). Implementation of hypoxia imaging into treatment planning and delivery. *Radiother Oncol* **97**, 172–175.

[40] Whisenant JG, Sorace AG, McIntyre JO, Hakmook K, Sánchez V, Loveless ME, and Yankeelov TE (2014). Evaluating treatment response using DW-MRI and DCE-MRI in trastuzumab responsive and resistant HER2-overexpressing human breast cancer xenografts. *Transl Oncol* **7**, 768–779.

[41] Moestue SA, Huuse EM, Lindholm EM, Bofin A, Engebraaten O, Mælandsmo GM, Akslen LA, and Gribbestad IS (2013). Low-molecular contrast agent dynamic contrast-enhanced (DCE)-MRI and diffusion-weighted (DW)-MRI in early assessment of bevacizumab treatment in breast cancer xenografts. *J Magn Reson Imaging* **38**, 1043–1053.

[42] Aliu SO, Wilmes LJ, Moasser MM, Hann BC, Li K-L, Wang D, and Hylton NM (2009). MRI methods for evaluating the effects of tyrosine kinase inhibitor administration used to enhance chemotherapy efficiency in a breast tumor xenograft model. *J Magn Reson Imaging* **29**, 1071–1079.

[43] Li X, Abramson RG, Arlinghaus LR, Kang H, Chakravarthy AB, Abramson VG, Farley J, Mayer IA, Kelley MC, and Meszoely IM, et al (2015). Multiparametric magnetic resonance imaging for predicting pathological response after the first cycle of neoadjuvant chemotherapy in breast cancer. *Investig Radiol* **50**, 195–204.

[44] Fangberget A, Nilsen LB, Hole KH, Holmen MM, Engebraaten O, Naume B, Smith H-J, Olsen DR, and Seierstad T (2011). Neoadjuvant chemotherapy in breast cancer-response evaluation and prediction of response to treatment using dynamic contrast-enhanced and diffusion-weighted MR imaging. *Eur Radiol* **21**, 1188–1199.

[45] Yankeelov TE, Lepage M, Chakravarthy A, Broome EE, Niermann KJ, Kelley MC, Meszoely I, Mayer IA, Herman CR, and McManus K, et al (2007). Integration of quantitative DCE-MRI and ADC mapping to monitor treatment response in human breast cancer: initial results. *Magn Reson Imaging* **25**, 1–13.

[46] He S, Wang M, Yang Z, Zhang J, Zhang Y, Luo J, and Zhang Y (2016). Comparison of 18F-FES, 18F-FDG, and 18F-FMISO PET imaging probes for early prediction and monitoring of response to endocrine therapy in a mouse xenograft model of ER-positive breast cancer. *PLoS One* **11**, 1–12.

[47] Mills SJ, O'Connor JPB, Buonaccorsi GA, Roberts C, Watson Y, Cheung S, Zhao S, Whitcher B, Jackson A, and Parker GJM (2009). Quantifying spatial heterogeneity in dynamic contrast-enhanced MRI parameter maps. *Magn Reson Med* **62**, 488–499.

[48] Baselga J, Norton L, Albanell J, Kim Y-M, and Mendelsohn J (1998). Recombinant humanized anti-HER2 antibody (Herceptin™) enhances the antitumor activity of paclitaxel and doxorubicin against HER2/neu overexpressing human breast cancer xenografts. *Cancer Res* **58**, 2825–2831.

[49] Lewis GD, Figari I, Fendly B, Wong WL, Carter P, Gorman C, and Shepard HM (1993). Differential responses of human tumor cell lines to anti-p185HER2 monoclonal antibodies. *Cancer Immunol Immunother* **37**, 255–263.

[50] Loveless ME, Halliday J, Liess C, Xu L, Dortch RD, Whisenant J, Waterton JC, Gore JC, and Yankeelov TE (2012). A quantitative comparison of the influence of individual versus population-derived vascular input functions on dynamic contrast enhanced-MRI in small animals. *Magn Reson Med* **67**, 226–236.

[51] Loveless ME, Lawson D, Collins M, Nadella MVP, Reimer C, Huszar D, Halliday J, Waterton JC, Gore JC, and Yankeelov TE (2012). Comparisons of the efficacy of a Jak1/2 inhibitor (AZD1480) with a VEGF signaling inhibitor (cediranib) and sham treatments in mouse tumors using DCE-MRI, DW-MRI, and histology. *Neoplasia* **14**, 54–64.

[52] Kety SS (1951). The theory and applications of the exchange of inert gas at the lungs and tissues. *Pharmacol Rev* **3**, 1–41.

[53] Tofts PS, Brix G, Buckley DL, Evelhoch JL, Henderson E, Knopp MV, Larsson HBW, Lee T-Y, Mayr NA, and Parker GJM, et al (1999). Estimating kinetic parameters from dynamic contrast-enhanced t1-weighted MRI of a diffusable tracer: Standardized quantities and symbols. *J Magn Reson Imaging* **10**, 223–232.

[54] Linkert M, Rueden CT, Allan C, Burel J-M, Moore W, Patterson A, Loranger B, Moore J, Neves C, and MacDonald D, et al (2010). Metadata matters: access to image data in the real world. *J Cell Biol* **189**, 777–782.

[55] Maley CC, Koelble K, Natrajan R, Aktipis A, and Yuan Y (2015). An ecological measure of immune-cancer colocalization as a prognostic factor for breast cancer. *Breast Cancer Res* **17**, 1–13.

[56] Crokart N, Radermacher K, Jordan BF, Baudelet C, Cron GO, Grégoire V, Beghein N, Bouzin C, Feron O, and Gallez B (2005). Tumor radiosensitization by antiinflammatory drugs: evidence for a new mechanism involving the oxygen effect. *Cancer Res* **65**, 7911–7916.

[57] Li K-L, Wilmes LJ, Henry RG, Pallavicini MG, Park JW, Hu-Lowe DD, McShane TM, Shalinsky DR, Fu Y-J, and Brasch RC, et al (2005). Heterogeneity in the angiogenic response of a BT474 human breast cancer to a novel vascular endothelial growth factor-receptor tyrosine kinase inhibitor: Assessment by voxel analysis of dynamic contrast-enhanced MRI. *J Magn Reson Imaging* **22**, 511–519.

[58] McCormack DR, Walsh AJ, Sit W, Arteaga CL, Chen J, Cook RS, and Skala MC (2014). In vivo hyperspectral imaging of microvessel response to trastuzumab treatment in breast cancer xenografts. *Biomed Opt Express* **5**, 2247–2261.

[59] Le X-F, Mao W, Lu C, Thornton A, Heymach JV, Sood AK, and Bast RC (2008). Specific blockade of VEGF and HER2 pathways results in greater growth inhibition of breast cancer xenografts that overexpress HER2. *Cell Cycle* **7**, 3747–3758.

[60] Hardee ME, Eapen RJ, Rabbani ZN, Dreher MR, Marks J, Blackwell KL, and Dewhirst MW (2009). Her2/neu signaling blockade improves tumor oxygenation in a multifactorial fashion in Her2/neu+ tumors. *Cancer Chemother Pharmacol* **63**, 219–228.

[61] Heyerdahl H, Røe K, Brevik EM, and Dahle J (2013). Modifications in dynamic contrast-enhanced magnetic resonance imaging parameters after α-particle–emitting 227Th-trastuzumab therapy of HER2-expressing ovarian cancer xenografts. *Int J Radiat Oncol* **87**, 153–159.

[62] Goel S, Wong AH-K, and Jain RK (2012). Vascular normalization as a therapeutic strategy for malignant and nonmalignant disease. *Cold Spring Harb Perspect Med* **2**, 1–24.

[63] Tolaney SM, Boucher Y, Duda DG, Martin JD, Seano G, Ancukiewicz M, Barry WT, Goel S, Lahdenrata J, and Isakoff SJ, et al (2015). Role of vascular density and normalization in response to neoadjuvant bevacizumab and chemotherapy in breast cancer patients. *Proc Natl Acad Sci* **112**, 14325–14330.

[64] Martin JD, Fukumura D, Duda DG, Boucher Y, and Jain RK (2016). Reengineering the tumor microenvironment to alleviate hypoxia and overcome cancer heterogeneity. *Cold Spring Harb Perspect Med* **6**, a027094.

[65] Bonnitcha P, Grieve S, and Figtree G (2018). Clinical imaging of hypoxia: current status and future directions. *Free Radic Biol Med* **126**, 296–312.